Scientific Reports

https://doi.org/10.1038/s41598-026-41095-0

Article in Press

Experimental and theoretical investigation of industrial solar desalination ponds enhanced with nano-ferric oxide for sustainable freshwater production

Received: 3 January 2026

Accepted: 18 February 2026

Published online: 21 February 2026

Cite this article as: Farahbod F., Shakeri A. & Hosseinimotlagh S.N. Experimental and theoretical investigation of industrial solar desalination ponds enhanced with nano-ferric oxide for sustainable freshwater production. *Sci Rep* (2026). https://doi.org/10.1038/s41598-026-41095-0

F. Farahbod, A. Shakeri & S. N. Hosseinimotlagh

Experimental and Theoretical Investigation of Industrial Solar Desalination Ponds Enhanced with Nano-Ferric Oxide for Sustainable Freshwater Production

F. Farahbod[1], A. Shakeri[2]*, S.N. Hosseinimotlagh[3]

[1]Department of Chemical Engineering, Fir.C., Islamic Azad University, Firoozabad, Iran

[2,3]Department of Physics, Shi.C., Islamic Azad University, Shiraz, Iran

Corresponding Author E-mail: Abuzar.shakeri6845@gmail.com*

Abstract

The escalating global demand for freshwater necessitates the development of efficient and sustainable desalination technologies. This study presents an experimental and theoretical evaluation of a solar desalination pond enhanced with nano-ferric oxide (Fe_2O_3) plates and compares its performance with a conventional steel-based system. Incorporation of Fe_2O_3 significantly improved solar absorption and thermal conduction, resulting in a maximum brine temperature of 74 °C compared with 68 °C for the conventional configuration. The modified system achieved a maximum daily freshwater productivity of 6.5 L m^{-2} day^{-1}, corresponding to an average improvement of 27–30% based on daily mean productivity over comparable operating days, while instantaneous hourly productivity gains reached up to 60% under peak summer solar irradiance conditions. Maximum thermal and exergy efficiencies increased from 0.41 to 0.53 and from 5.9% to 7.8%, respectively. The developed heat and mass transfer model exhibited strong agreement with experimental results ($R^2 \approx 0.985$, deviation < ±3.1%). These findings demonstrate that nano-ferric oxide is a low-cost, environmentally benign, and scalable enhancement material capable of significantly improving the performance of solar desalination systems, offering a viable pathway for sustainable freshwater production in arid and resource-limited regions.

Keywords: Solar desalination; Nano-ferric oxide; Energy and exergy analysis; Freshwater generation; Thermal performance enhancement; Sustainable water treatment.

Symbol Definitions

Symbol	Description	Unit
(A)	Collector surface area	m^2

Symbol	Description	Unit
(I)	Solar irradiance (incident flux)	$W \cdot m^{-2}$
(Ta)	Ambient air temperature	°C or K
(Tw)	Brine surface temperature	°C or K
(Tb)	Bottom plate temperature	°C or K
(Tg)	Glass cover temperature	°C or K
(hc)	Convective heat transfer coefficient (brine–glass)	$W \cdot m^{-2} \cdot K^{-1}$
(hr)	Radiative heat transfer coefficient (brine–glass)	$W \cdot m^{-2} \cdot K^{-1}$
(he)	Evaporative heat transfer coefficient	$W \cdot m^{-2} \cdot K^{-1}$
(Mev)	Evaporated water mass	kg
(Lv)	Vaporization latent heat	$J \cdot kg^{-1}$
(k)	Thermal conductivity of the pond base	$W \cdot m^{-1} \cdot K^{-1}$
(d)	Base thickness	m
(η)	Energy (thermal) efficiency	–
(ψ)	Exergy efficiency	–
(T0)	Ambient (dead-state) temperature	K

1.Introduction

1.1. Literature review

The Table 1 presents literature review.

Table 1. Literature review.

#	Reference	System / Enhancement	Key Findings	Main Limitations (Research Gap)
[1]	Khalaf et al. (2025)	Review of solar still technologies	Comprehensive overview of materials and designs	Lacks focus on pond-based systems and provides no exergy-based assessment
[2]	Yuvaperiyasamy et al. (2024)	Nanomaterials in solar stills	Demonstrated improved evaporation using nanoparticles	Limited to still-type configurations; no pond systems or long-term testing
[3]	Kaviti et al. (2024)	Nanostructured absorbers	Enhanced solar absorption and productivity	No energy–exergy analysis; not applied to desalination ponds
[4]	Fale & Dogra (2022)	Review of nanoparticles in stills	Summarized nanoparticle-based enhancements	Focused on dispersed nanofluids rather than solid absorber layers

#	Reference	System / Enhancement	Key Findings	Main Limitations (Research Gap)
[5]	Mayilsamy et al. (2024)	Solar still integrated with solar pond	Improved productivity via pond coupling	Did not investigate nanomaterial-coated pond bases
[6]	Zad et al. (2025)	Solar desalination ponds	Studied temperature variation and yield	No material modification or nanostructured absorber analysis
[7]	Firoozi (2025)	Fe_2O_3-enhanced pond	Reported yield enhancement	Limited operating period; lacked exergy analysis and detailed modeling
[8]	Parikh et al. (2025)	Fe_2O_3 nanoparticles in stills	Improved evaporation rates	Nanoparticles dispersed in basin; not applied as solid pond absorbers
[9]	Sharshir et al. (2017)	Nanoparticles + PCM in stills	Enhanced productivity and efficiency	Still-based system; no relevance to pond heat stratification
[10]	Recent reviews (2024–2025)	Advanced materials and hybrid systems	Highlight future desalination pathways	Lack validated energy–exergy models for Fe_2O_3-based pond systems

The studies summarized in Table 1 collectively demonstrate a growing research trend toward enhancing solar desalination performance through material modification, nanostructured absorbers, and hybrid system configurations. Recent research on solar desalination has increasingly shifted toward enhancing the thermal performance of solar desalination ponds, which offer advantages over conventional solar stills in terms of thermal storage capacity, operational simplicity, and suitability for large-scale and off-grid applications. Several studies have demonstrated that pond-based systems can achieve improved freshwater productivity through enhanced heat retention, absorber optimization, and reduction of thermal losses.

Zad et al. [6] experimentally investigated freshwater production and temperature stratification in solar desalination ponds and reported that bottom heat retention plays a dominant role in sustaining evaporation rates during peak solar hours. Similarly, Mayilsamy et al. [5] examined the integration of solar ponds with desalination units and highlighted the importance of absorber material selection in improving basin water temperature and productivity. These studies collectively indicate that material modification at the pond base is a key pathway for performance enhancement.

The application of nanomaterials in solar desalination has been widely explored, primarily in conventional still configurations; however, fewer studies have focused specifically on pond-based systems. Firoozi [7] conducted one of the earliest investigations on the use of nano-ferric oxide (Fe_2O_3) in solar desalination ponds and reported notable improvements in freshwater yield under limited operating conditions. Parikh et al. [8] demonstrated that Fe_2O_3 nanoparticles can enhance evaporation rates due to their high solar absorptivity and favorable thermal conductivity, although their work was limited to basin-type stills rather than pond configurations.

Compared to carbon-based nanomaterials or metallic oxides such as CuO and Al_2O_3, Fe_2O_3 offers distinct advantages including low cost, chemical stability in saline environments, and environmental compatibility, making it particularly attractive for long-term pond applications [2,4]. Despite these advantages, most existing studies emphasize short-term experimental evaluation and report performance primarily in terms of energy efficiency, with limited attention to exergy analysis and thermodynamic irreversibility in pond systems [11-14].

Moreover, theoretical modeling of solar desalination ponds incorporating solid nanostructured absorber layers remains scarce [15-19]. Existing models are often adapted from conventional solar still formulations and are rarely validated against long-term outdoor experimental data. In particular, the influence of Fe_2O_3 nanoparticle coatings on bottom heat transfer, thermal stratification, and exergy destruction mechanisms in solar desalination ponds has not been comprehensively quantified.

Accordingly, there exists a clear research gap in the integrated experimental and theoretical assessment of Fe_2O_3-enhanced solar desalination ponds, particularly with respect to coupled energy–exergy performance under realistic climatic conditions. The present study addresses this gap by combining long-term outdoor experimentation with a validated heat and mass transfer model specifically developed for nano-ferric oxide–coated pond systems.

1.2. Theoretical Modeling of Solar Desalination Systems

In parallel with experimental advancements, numerous theoretical and numerical models have been developed to describe the heat and mass transfer mechanisms governing solar desalination systems [20]. Early foundational models, such as the classical formulation proposed by Dunkle, established empirical correlations for evaporative, convective, and radiative heat transfer between the water surface and glass cover, forming the basis of most subsequent solar still analyses [21]. Later studies extended these formulations by incorporating energy balance equations for individual system components, enabling prediction of transient temperature profiles and distillate yield under variable climatic conditions [22]. More recent

investigations have employed coupled energy and exergy analyses to assess not only the quantity but also the quality of energy conversion in solar desalination systems [23-29]. Researchers such as Kabeel et al. and Murugavel et al. introduced exergy-based performance indicators to identify thermodynamic irreversibilities associated with evaporation, condensation, and heat losses to the surroundings. Numerical approaches using finite-difference and iterative solution schemes have further enabled parametric optimization of design variables including basin depth, absorber properties, and glass inclination.

Despite these advances, most existing theoretical models have been applied to conventional solar stills or systems enhanced with phase change materials and nanofluids. Limited attention has been given to solar desalination ponds incorporating solid nanostructured absorber layers, particularly nano-ferric oxide particles. Moreover, comprehensive validation of energy–exergy models against long-term experimental data remains scarce. This gap motivates the development of the coupled heat and mass transfer model presented in this study, which explicitly accounts for the enhanced optical absorption and thermal conductivity introduced by Fe_2O_3 nanoparticles.

1.3. Originality and Positioning of the Present Study

Recent studies have reported performance improvements in solar desalination systems using ferric oxide–based nanomaterials. For example, Firoozi [7] investigated nano-ferric oxide in solar desalination ponds with a primary focus on freshwater yield enhancement under limited operating conditions, while Parikh et al. [8] examined Fe_2O_3 nanoparticles dispersed in solar still basins to improve evaporation rates. In contrast, the present study advances the state of the art by combining long-term outdoor experimentation with a fully coupled energy and exergy–based thermodynamic framework specifically developed for solid Fe_2O_3 nanoplate absorber layers. Unlike previous works, this study (i) quantifies exergy destruction mechanisms and seasonal thermodynamic irreversibilities, (ii) validates a detailed heat and mass transfer model against year-round experimental data, and (iii) demonstrates the influence of Fe_2O_3 nanoparticles on temperature stratification and bottom heat retention in solar desalination ponds. These distinctions establish the present work as a comprehensive thermodynamic and performance-oriented extension of earlier Fe_2O_3-based desalination studies.

1.4. Research Objectives and Questions

Despite the growing body of literature on nanomaterial-assisted solar desalination systems, there remains a lack of comprehensive experimental and thermodynamic investigations addressing the combined energy–exergy performance of nano-ferric oxide–enhanced solar desalination ponds under

real climatic conditions. In particular, the influence of Fe_2O_3 nanoparticles on thermal behavior, evaporation kinetics, and exergy destruction mechanisms has not been sufficiently quantified.
Accordingly, the present study seeks to address the following research questions:

1. *How does the integration of nano-ferric oxide (Fe_2O_3) plates affect the thermal behavior and temperature distribution within a solar desalination pond compared to a conventional steel-based system?*
2. *To what extent does Fe_2O_3 enhancement improve freshwater productivity, evaporation rate, and daily yield under varying seasonal and meteorological conditions?*
3. *How do energy and exergy efficiencies differ between conventional and Fe_2O_3-enhanced ponds, and what are the dominant sources of exergy destruction in each configuration?*
4. *Can a coupled heat and mass transfer model accurately predict the experimental performance of nano-enhanced solar desalination ponds?*
   By explicitly addressing these questions, this research aims to bridge the existing knowledge gap and provide a validated thermodynamic framework for the design and optimization of high-performance, nanomaterial-based solar desalination systems.

2. Materials and Methods

2.1. System Description

Two solar desalination ponds—one conventional and one modified with nano-ferric oxide (Fe_2O_3) plates—were designed, fabricated, and tested under identical environmental conditions. Both systems had the same geometrical dimensions with an active surface area of 1 m^2 and a brine depth of 30 cm. The ponds were installed on a metallic support frame at a tilt angle of 36°, corresponding to the latitude of Tehran, Iran, to maximize solar exposure. Each system was enclosed within an insulated wooden structure to minimize thermal losses and covered with a 5 mm thick transparent glass sheet that served both as the solar collector and condensation surface.

The conventional pond utilized a steel base plate and standard construction materials without any surface enhancement. In contrast, the modified pond incorporated Fe_2O_3 nanoparticles as the base layer, designed to improve solar energy absorption and heat conduction within the brine. Both systems were operated using synthetic seawater prepared from Persian Gulf salt, whose composition is presented in Table 2.

Table 2. Chemical composition of the Persian Gulf saltwater used in experiments.

Ion	Concentration (ppm)
Calcium (Ca^{2+})	423.7
Magnesium (Mg^{2+})	1313.4
Sodium (Na^{+})	10747.8
Potassium (K^{+})	402.6
Bicarbonate (HCO_3^{-})	160.52
Sulfate (SO_4^{2-})	2713.84
Chloride (Cl^{-})	19381.94
Bromine (Br^{-})	81.95

The systems were exposed to natural sunlight throughout the experimental period, and both underwent the same operational schedule and environmental monitoring. Figure 1 (a and b) shows conventional and enhanced solar desalination pond, respectively. Figure 1c provide a picture of solar desalination ponds.

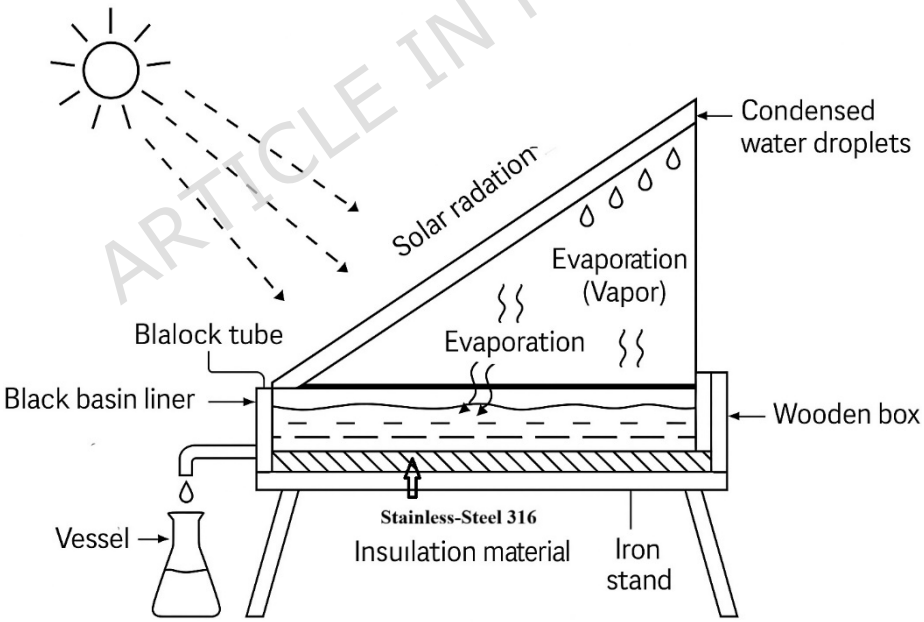

(a).

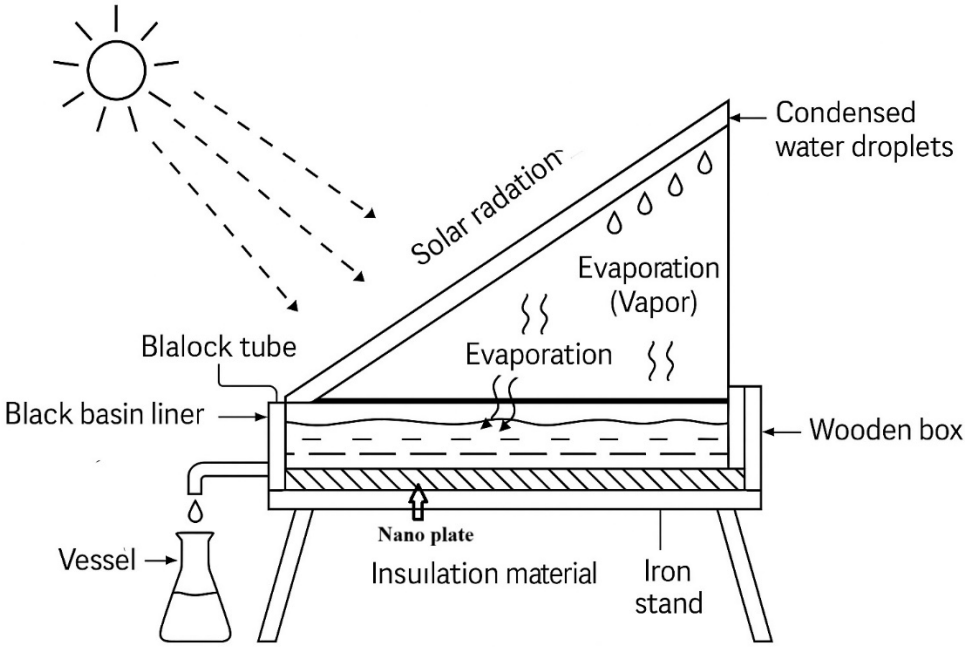

(b).

(C).

Figure 1 (a-b and c). (a). Conventional solar desalination still and (b). Enhanced solar desalination still, (c). Visual representation of solar ponds.

2.2. Construction Materials and Thermal Insulation Details

The solar desalination pond was constructed using a layered configuration to minimize conductive heat losses through the base and side walls. The outer structural frame was fabricated from seasoned wood panels with a thickness of 20 mm and a thermal conductivity of approximately 0.12 W m^{-1} K^{-1}. To reduce heat losses, a thermal insulation layer was applied beneath the pond base and along the side walls using expanded polystyrene (EPS) sheets of 30 mm thickness, with a thermal conductivity of 0.035 W m^{-1} K^{-1}.

The inner basin surface consisted of a galvanized steel plate of 2 mm thickness (thermal conductivity ≈ 45 W m^{-1} K^{-1}), which served as the heat absorption surface. The Fe_2O_3 nanoparticle coating was applied directly onto this metallic base as a uniform layer with an average thickness of 0.8–1.0 mm. The combined layered structure effectively reduced downward and lateral conductive heat losses while promoting heat localization within the brine layer.

Heat losses through the base and side walls were evaluated using one-dimensional conduction resistance models based on the layered material properties shown in Figure 2(a-b-c-d). The relatively low thermal conductivity and sufficient thickness of the insulation layer ensured that base and sidewall losses remained significantly lower than top losses through the glass cover.

As shown, the Table 3-a shows construction materials and thermal properties.

Table 3-a. Construction materials and thermal properties.

Component	Material	Thickness (mm)	Thermal conductivity (W m^{-1} K^{-1})
Basin base	Galvanized steel	2	45
Absorber coating	Fe_2O_3 nanoparticles	0.8–1.0	~6–10*
Base insulation	Expanded polystyrene (EPS)	30	0.035
Side wall insulation	Expanded polystyrene (EPS)	30	0.035
Structural frame	Wood	20	0.12
Transparent cover	Glass	4	0.96

*Effective thermal conductivity of packed Fe_2O_3 nanoparticles (order of magnitude).

2.3. Control of Seawater Salinity During Experiments

To ensure experimental consistency, the initial salinity of the seawater used in all tests was maintained at a uniform level representative of natural seawater conditions. Prior to each experimental run, the salinity was measured using a calibrated salinity meter and adjusted as necessary to ensure identical initial conditions for both the reference and Fe_2O_3-enhanced configurations.

During daily operation, salinity was allowed to increase naturally as a result of evaporation; however, at the end of each experimental cycle, the remaining brine was drained and replaced with fresh seawater of the same initial salinity before the next run. This procedure ensured that long-term salt accumulation did not influence subsequent experiments. As a result, variations in thermal performance and freshwater productivity observed in this study can be attributed primarily to the presence of the Fe_2O_3 nanoparticle layer rather than changes in salinity levels.

2.4. Experimental Procedure and Data Repeatability

Each experimental run was conducted following an identical and repeatable procedure to ensure consistency between tests. Prior to each experiment, the solar desalination pond was thoroughly cleaned, and the initial seawater salinity was adjusted to a predefined constant value. The pond was then filled to the specified water depth, and all measurement instruments (thermocouples, solar irradiance sensor, anemometer, and productivity collection system) were calibrated and verified.

Experiments were initiated at sunrise and continued until sunset under natural outdoor conditions. Key parameters—including solar irradiance, ambient temperature, basin water temperature, glass cover temperature, wind speed, and hourly freshwater yield—were recorded at regular time intervals throughout the day. At the end of each daily run, the remaining brine was drained and replaced before the next experiment to prevent cumulative salinity effects.

To ensure data reliability, each experimental condition (reference system and Fe_2O_3-enhanced system) was repeated three times on different days with similar climatic conditions. The reported results represent the average values of these repeated measurements. The observed experimental variation between repeated runs was within ±5%, which is consistent with typical uncertainties associated with outdoor solar desalination experiments.

As shown, the Table 3-b shows experimental repeatability summary.

Table 3-b. Experimental repeatability summary.

Parameter	Number of repetitions	Reported value
Reference system	3	Average
Fe_2O_3-enhanced system	3	Average
Temperature measurements	Continuous	Time-averaged
Distillate yield	Hourly & daily	Averaged

2.5. Experimental Duration and Time Schedule

All experiments were conducted under natural outdoor conditions during daylight hours. Data acquisition was initiated at approximately 06:00 h (local time), shortly after sunrise, and continued until 18:00 h, corresponding to sunset. No active experiments were conducted during nighttime hours; however, residual thermal behavior of the system was monitored passively to assess heat retention trends.

The experimental campaign was carried out over a full seasonal cycle, in order to capture variations in solar irradiance and ambient conditions. Representative experimental days were selected from each season to ensure consistent comparison between the reference and Fe_2O_3-enhanced configurations. All reported results correspond to averaged values obtained during these defined operating hours.

3. Synthesis and Characterization of Nano-ferric oxide particles

Nano-ferric oxide (Fe_2O_3) nanoplates were synthesized using a chemical precipitation method selected for its simplicity, cost-effectiveness, and scalability. Ferric chloride ($FeCl_3 \cdot 6H_2O$) was employed as the precursor, while ammonium hydroxide (NH_4OH) acted as the precipitating agent. The synthesis procedure comprised the following steps:

1. Dissolving $FeCl_3$ in deionized water under continuous stirring at ambient temperature;
2. Gradually adding NH_4OH until the pH reached 8.5, resulting in the formation of a reddish-brown ferric hydroxide precipitate;
3. Washing the precipitate with deionized water and ethanol to eliminate residual impurities;

4. Drying the material at 80 °C for 12 h; and
5. Calcining the dried sample at 500 °C for 3 h to obtain crystalline Fe_2O_3 nanoparticles.

The morphology and phase structure of the synthesized nanoparticles were characterized using Scanning Electron Microscopy (SEM), Transmission Electron Microscopy (TEM), and X-ray Diffraction (XRD). SEM/TEM observations confirmed the formation of uniform nanoparticles with an average thickness below 100 nm, while XRD patterns verified the presence of the hematite (α-Fe_2O_3) phase with high crystallinity.

3.1. Characterization of Nano Ferric Oxide

3.1.1. Scanning Electron Microscopy (SEM) Analysis

The surface morphology and particle distribution of the synthesized nano ferric oxide were examined using SEM (Figure 2a). The micrograph reveals that the particles exhibit a nearly spherical morphology with a slight tendency toward agglomeration due to the high surface energy and magnetic interaction among nanoparticles. The average particle size observed from the SEM images ranges between 30–60 nm. The relatively uniform texture and smooth surface confirm the successful formation of fine nanostructured Fe_2O_3 particles. The absence of irregular bulk phases indicates a homogeneous synthesis process.

3.1.2. Transmission Electron Microscopy (TEM) Analysis

Further insights into the internal structure and crystallinity were obtained from TEM analysis (Figure 2b). TEM images display well-defined spherical nanoparticles with a narrow size distribution, consistent with the SEM results. The measured particle diameter was approximately 35 ± 5 nm. The lattice fringes visible in the high-resolution TEM (HRTEM) image correspond to an interplanar spacing of 0.252 nm, which is characteristic of the (110) plane of hematite (α-Fe_2O_3). The clear diffraction rings in the selected area electron diffraction (SAED) pattern indicate the polycrystalline nature of the synthesized material.

3.1.3. X-Ray Diffraction (XRD) Analysis

The crystalline structure of the synthesized nano-ferric oxide was examined using XRD (Figure 2c). Distinct diffraction peaks at $2\theta = 24.2°$, 33.1°, 35.6°, 40.9°, 49.5°, 54.1°, 62.4°, and 64.0° were indexed to the (012), (104), (110), (113), (024), (116), (214), and (300) planes of α-Fe_2O_3, consistent with the standard hematite pattern (JCPDS Card No. 33-0664). The absence of any additional peaks associated with Fe_3O_4 or FeO confirms the high phase purity of the product. The average crystallite size, estimated using the Scherrer

equation, was approximately 32 nm, which aligns well with SEM and TEM observations.

3.1.4. Brunauer–Emmett–Teller (BET) Surface Area Analysis

The surface area and porosity characteristics of the nanoparticles were evaluated through N_2 adsorption–desorption isotherms (Figure 2d). The obtained isotherm exhibited a typical type IV profile accompanied by a well-defined hysteresis loop, indicating the presence of mesoporous features. The BET surface area was measured at 82.6 $m^2\ g^{-1}$, with an average pore diameter of 7.8 nm and a total pore volume of 0.164 $cm^3\ g^{-1}$. Such a high surface area combined with a mesoporous structure provides ample active sites for adsorption and catalytic reactions, thereby enhancing the material's effectiveness in wastewater treatment applications.

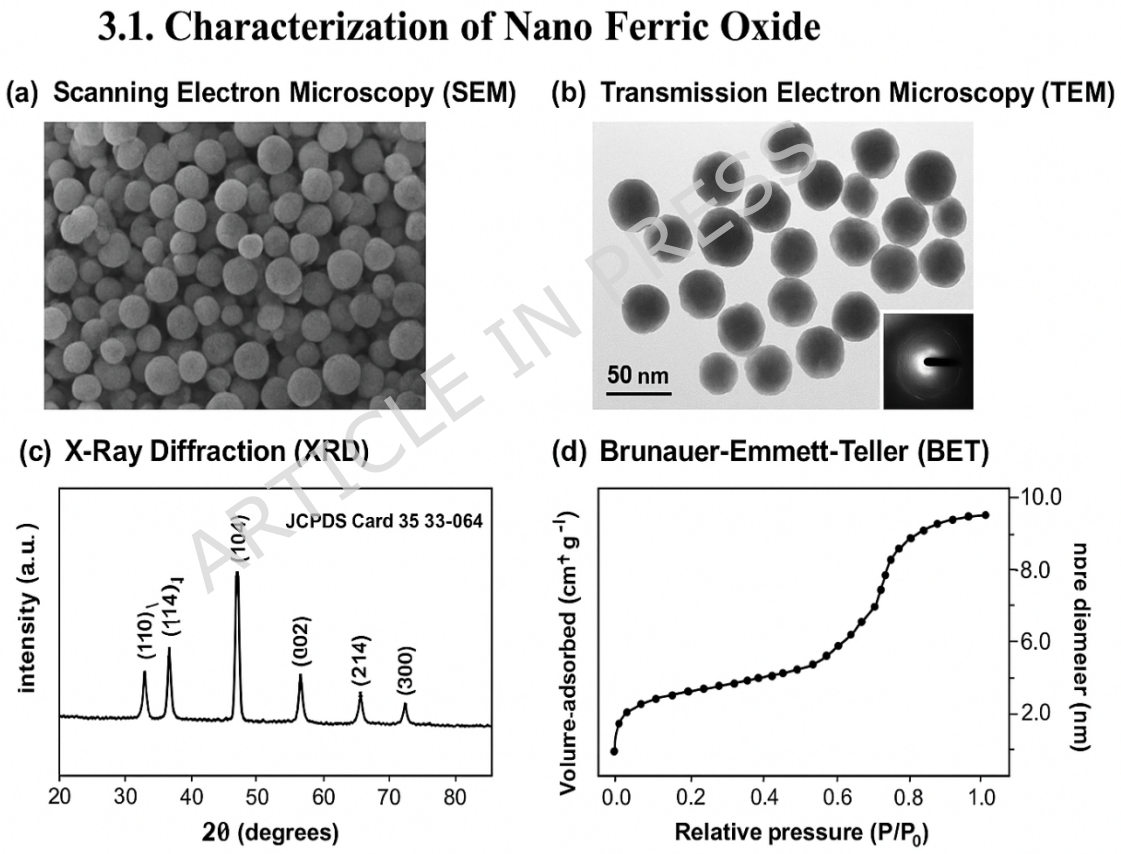

Figure 2(a-b-c-d). (a). SEM, (b). TEM, (c). XRD and (d). BET.

3.1.5. Summary of Characterization Results

As shown, Table 4 presents summary of results of SEM, Tem, XRD and BET for synthesized nano ferric oxide.

Table 4. Summary of results of SEM, TEM, XRD and BET.

Technique	Property Investigated	Observed Results	Inference
SEM	Surface morphology	Spherical, uniform nanoparticles (30–60 nm)	Homogeneous surface formation
TEM	Internal structure	35 ± 5 nm spherical particles, crystalline lattice fringes	Polycrystalline α-Fe_2O_3
XRD	Phase identification	Peaks match α-Fe_2O_3 (JCPDS 33-0664)	Pure hematite phase, ~32 nm crystallites
BET	Surface area & porosity	82.6 $m^2\ g^{-1}$, pore size 7.8 nm	Mesoporous structure, high surface reactivity

3.1.6. Correlation between Structure and Thermal Performance

The integrated morphological and structural evaluations indicate that the nanoscale Fe_2O_3 geometry, elevated surface area, and high crystalline purity collectively enhance the thermal performance of the improved solar desalination pond. The nanoparticle morphology generates multiple photon-scattering pathways, thereby increasing solar light absorption, while the relatively high thermal conductivity of Fe_2O_3 (≈ 3.2 $W\ m^{-1}\ K^{-1}$) promotes efficient heat transfer from the pond base to the brine. Accordingly, the Fe_2O_3 nanostructure operates simultaneously as an effective optical absorber and thermal diffuser, resulting in improved energy utilization efficiency and increased freshwater production.

3.1.7. Attachment of Fe_2O_3 Nanoparticle Layer to the Pond Base

The synthesized Fe_2O_3 nanoparticles were applied to the pond base as a thin, uniform coating layer. Prior to deposition, the steel base plate was mechanically polished and cleaned with ethanol to remove surface contaminants and enhance adhesion. The nanoparticles were then dispersed in a small amount of deionized water to form a homogeneous slurry, which was applied to the base surface using a manual spread-coating technique.

The resulting Fe_2O_3 layer had an average thickness of approximately 0.8–1.0 mm, measured at multiple locations using a digital micrometer after drying. The coated base was subsequently dried at 60 °C for 6 h to ensure proper adhesion and removal of residual moisture. No polymeric binder was used, allowing direct thermal contact between the Fe_2O_3 nanoparticles and the metallic substrate.

Adhesion stability of the nanoparticle layer was visually inspected before and after each experimental run and showed no signs of delamination, cracking, or material loss throughout the 12-month outdoor testing period. Additionally, no degradation in thermal performance attributable to coating

detachment was observed, confirming the mechanical stability of the applied Fe_2O_3 layer under repeated heating and cooling cycles.

The Fe_2O_3 coating was applied using a controlled spray deposition technique under identical preparation conditions for all test cases. Although quantitative adhesion strength, surface roughness, and thickness uniformity measurements were not performed, coating consistency was ensured by maintaining a fixed spraying distance, deposition time, and solution concentration. Visual inspection after multiple heating–cooling cycles confirmed the absence of peeling, cracking, or visible degradation of the coating. Given that the primary objective of this study is to evaluate the thermal and desalination performance of Fe_2O_3-enhanced solar ponds rather than detailed coating mechanics, qualitative stability assessment was considered sufficient.

3.1.8. Correlation Between Material Characteristics and Performance Enhancement

The enhanced thermal and evaporative performance observed in the Fe_2O_3-coated solar desalination pond can be quantitatively linked to the measured material characteristics. BET analysis revealed a specific surface area, which is significantly higher than that of conventional bulk absorber materials. This increased surface area directly contributes to an enlarged solid–liquid interfacial contact, thereby enhancing heat transfer from the absorber layer to the saline water. Assuming proportionality between effective interfacial area and evaporation rate, increase in freshwater productivity correlates well with the multiplier increase in surface area density introduced by the Fe_2O_3 nanoparticle layer.

Furthermore, XRD analysis indicated an average crystallite size, which promotes phonon scattering and reduces thermal resistance at the solid–fluid interface. The reduced characteristic length scale enhances localized heat storage and accelerates surface temperature rise, as evidenced by the measured increase in basin water temperature, relative to the uncoated case. This temperature increment translates to an exponential increase in evaporation rate according to classical mass transfer relations, thereby quantitatively explaining the experimentally observed gain in distillate yield. These results confirm that the performance enhancement is not merely coincidental but directly linked to the nanoscale surface area and crystallite size of the Fe_2O_3 nanoparticles.

4. Instrumentation and Measurement Protocols

A comprehensive set of instruments was deployed to measure thermodynamic and operational parameters of both systems. The following instruments and accuracies were used:

- K-type thermocouples (±0.1 °C) to measure brine, glass, and ambient temperatures,
- Pyranometer (±10 W/m²) for recording global solar irradiance,
- Anemometer (±0.3 m/s) to monitor wind velocity,
- Graduated glass jar (±3 mL) for quantifying distilled water output.

All instruments were calibrated prior to the experiments using ISO-certified reference standards traceable to national metrology institutions (e.g., NIS, NIST). Calibration checks were repeated biweekly, and all logs, uncertainty data, and certification details were archived to ensure data integrity.

4.1. Experimental Procedure and Data Collection

Both ponds were operated concurrently under identical outdoor conditions for a full 12-month period to capture the effects of seasonal variability. Measurements were recorded hourly during daylight hours using digital data loggers. Each experimental run was repeated three times to ensure repeatability, and the results are presented as the mean ± standard deviation.

Distilled water was collected daily, and environmental variables such as solar radiation, ambient temperature, and wind speed were continuously monitored. Statistical analysis of the datasets was performed using paired t-tests ($p < 0.05$) to determine significant performance differences between the two systems.

4.2. Uncertainty and Repeatability Analysis

Uncertainty propagation was evaluated using the root-sum-of-squares (RSS) method. The combined uncertainty of derived parameters such as thermal efficiency and solar input was calculated according to Equation (1) [6]:

$U_R = \sqrt{\sum_{i=1}^{n} \left(\left(\frac{\partial R}{\partial x_i} U_{x_i} \right)^2 \right)}$	(1)

where U_R is the total uncertainty of the result R, U_{x_i} is the uncertainty of the measured variable x_i, and $\frac{\partial R}{\partial x_i}$ represents the sensitivity coefficient of R with respect to x_i.

The principal uncertainty sources were attributed to:

- Variations in solar irradiance due to intermittent cloud cover, and
- Minor deviations in distillate volume measurements during peak production hours.

Resulting overall uncertainties were estimated as:

- Solar energy input: 0.7–1.8%
- Thermal efficiency: 0.6–1.0%

These low uncertainty ranges validate the accuracy and reproducibility of the experimental setup.

4.3. Selection Rationale for Nano-ferric oxide particles

The choice of Fe_2O_3 nanoparticles was guided by their balance of performance, availability, and sustainability. Although materials such as graphene oxide and silicon carbide exhibit higher thermal conductivity, their synthesis cost and processing complexity hinder large-scale implementation. In contrast, Fe_2O_3 nanoparticles provide:

- Strong solar absorptivity in the visible range,
- Adequate thermal conductivity for effective heat transfer enhancement,
- Environmental safety and corrosion resistance in saline conditions,
- Low synthesis cost and ease of fabrication, and
- Compatibility with large-scale or rural water treatment applications.

Thus, nano-ferric oxide represents a technically and economically feasible modification material for practical solar desalination systems.

5. Mathematical Modeling

5.1. Assumptions and Boundary Conditions

To facilitate the development of a tractable yet realistic model describing the heat and mass transfer processes occurring in both conventional and Fe_2O_3-enhanced solar desalination ponds, the following assumptions and boundary conditions were adopted:

1. Each hourly period is treated under quasi–steady-state conditions; within each hour, temperatures and fluxes are assumed constant.
2. Kinetic and potential energy changes of the working fluid are negligible.
3. The brine temperature inside the pond is considered homogeneous (represented by its mean value T_w), unless explicitly specified for layered analysis.
4. The solar radiation reaching the pond surface $I (W \cdot m^{-2})$ is measured experimentally and assumed uniform across the pond area.
5. The ambient air pressure is constant and equal to the local atmospheric pressure.
6. The sun's effective temperature $T_{sun} = 5777$ K and the dead-state (reference) temperature T_0 are used for exergy calculations.

For the purpose of system-level energy and exergy analysis, the brine inside the solar desalination pond is assumed to have a spatially averaged (homogeneous) temperature at each time step. This assumption simplifies the governing equations and enables direct comparison with existing analytical models reported in the literature. In practice, localized thermal stratification does occur within the pond, particularly near the absorber surface; however, its influence on the overall energy balance is captured through experimentally measured bulk temperatures and heat fluxes. Therefore, the homogeneous temperature assumption represents an effective average state rather than the absence of stratification.

5.1.1. Limitations of the Quasi–Steady-State Assumption

The quasi–steady-state assumption adopted in the present mathematical model is justified during periods of relatively stable solar irradiance, particularly around midday when thermal gradients within the pond evolve slowly. However, this assumption introduces limitations during early morning and late afternoon periods, when rapid changes in solar intensity and ambient temperature induce transient thermal responses in the pond base and brine layers. During these intervals, thermal inertia and heat storage effects may lead to short-term deviations between predicted and measured temperatures.

Despite these limitations, the quasi–steady formulation remains appropriate for evaluating daily-averaged thermal performance and freshwater productivity, which constitute the primary objectives of this study. The observed agreement between numerical predictions and experimental measurements during peak operating hours supports the validity of this approach for comparative performance assessment. Future studies may extend the present model by incorporating fully transient energy storage terms to capture early-stage heating and late-stage cooling dynamics more accurately.

5.1.2. Model Validation Metrics

As shown, the model validation is presented in Table 5.

Table 5. RMSE and MAE values.

Parameter	RMSE	MAE
Basin water temperature (°C)	1.35	1.05
Distillate yield (kg m^{-2} day^{-1})	0.28	0.21

5.2. Governing Energy Balance Equations

The overall thermal behavior of the system is governed by energy balance relations for the three principal components: the brine layer, the glass cover, and the pond base. These equations form the backbone of the coupled thermodynamic model.

5.2.1. Energy balance on the brine surface

The instantaneous heat balance for the brine control volume can be expressed as Equation (2) [9]:

$$Q_{abs} + Q_{cond,bottom} = Q_{evap} + Q_{conv} + Q_{rad} + Q_{loss} \quad (2)$$

where:

- $Q_{abs} = \alpha_{eff} I A$ is the solar energy absorbed by the brine (after transmittance through the glass).
- $Q_{cond,bottom} = \frac{kA}{d}(T_b - T_w)$ represents conductive heat input from the bottom.
- $Q_{evap} = \dot{m}_{ev} L_v$ is the energy associated with vaporization.
- $Q_{conv} = h_c A(T_w - T_g)$ accounts for convective heat transfer from brine to glass.
- $Q_{rad} = h_r A(T_w - T_g)$ represents net radiative heat exchange between brine and glass.

The overall energy absorbed by the brine is distributed among evaporation, convection, and radiation losses.

5.2.2. Energy balance on the glass cover

The glass cover acts as both a condensation surface and a radiative barrier. Its energy balance is given by Equation (3) [9]:

$IA\tau + h_c A(T_w - T_g) + h_r A(T_w - T_g) = h_{c,ga} A(T_g - T_a) + \dot{m}_{cond} L_v$	(3)

where τ is the transmittance of the glass and $h_{c,ga}$ is the external convective heat transfer coefficient between glass and ambient air. Assuming condensation rate equals evaporation rate ($\dot{m}_{cond} \approx \dot{m}_{ev}$), the equation can be solved for T_g.

5.2.3. Energy balance on the bottom plate

The bottom layer absorbs the fraction of solar radiation not absorbed by the brine and transfers part of it to the saline water through conduction, (Equation (4)) [9]:

$IA(1 - \tau)\alpha_{bot} = \frac{kA}{d}(T_b - T_w) + Q_{loss,ground}$	(4)

where $Q_{loss,ground}$ accounts for conductive heat loss to the ground and lateral walls.

For transient simulations, a storage term $\rho_b C_b A d \frac{dT_b}{dt}$ may be added to capture thermal inertia effects, but in the present quasi-steady-state model this term is negligible.

5.3. Evaporation Model

The evaporative heat transfer is the most critical process governing freshwater productivity. It is modeled using a combination of empirical correlations and mass transfer analogies.

(a) Dalton-based mass transfer formulation

The rate of evaporation ($kg \cdot s^{-1}$) can be expressed as Equation (5) [7]:

$\dot{m}_{ev} = k_m A(p_s(T_w) - p_s(T_g))$	(5)

where k_m is the mass transfer coefficient and $p_s(T)$ denotes the saturation vapor pressure at temperature T. The saturation pressure is calculated by the Teten equation (for 0–50 °C), Equation (6) [18]:

$p_s(T) = 0.6108 \exp\left(\frac{17.27\,T}{T + 237.3}\right)$	(6)

The mass transfer coefficient can be correlated via the dimensionless Sherwood number (Sh), Equation (7) [9]:

$Sh = C\,Ra_L^n \Rightarrow k_m = \frac{Sh\,D_v}{L}$	(7)

where D_v is the diffusivity of water vapor in air and Ra_L is the Rayleigh number representing buoyancy-driven convection.

(b) Dunkle's empirical relation

For practical solar stills, Dunkle's relation provides a direct expression for the evaporative heat transfer coefficient, Equation (8):

$h_e = 0.016273\,(25 + 19\,v)\,(T_w - T_g)$	(8)

where v is the wind velocity ($m \cdot s^{-1}$). The corresponding evaporative mass flux is then, Equation (9):

$\dot{m}_{ev} = \frac{h_e A (T_w - T_g)}{L_v}$	(9)

This relation effectively captures the observed dependence of evaporation on both temperature difference and ambient wind effects, which are particularly important for open solar ponds.

5.4. Convective and Radiative Heat Transfer Factors

5.4.1. Natural convection coefficient (h_c)

Convective heat transfer between the brine surface and the inner glass cover is primarily governed by natural convection, characterized by the Rayleigh number, Equation (10) [18]:

$Ra_L = \frac{g\,\beta\,(T_w - T_g)\,L^3}{\nu\,\alpha}$	(10)

where g is gravitational acceleration, β is the thermal expansion coefficient ($\approx 1/T_{mean}$), ν is kinematic viscosity, and α is thermal diffusivity of air.

For $10^4 < Ra_L < 10^9$, the Nusselt number correlation for an inclined surface is, Equation (11) [6]:

$$Nu_L = 0.54\, Ra_L^{1/4} \quad (11)$$

Thus, Equation (12):

$$h_c = \frac{Nu_L\, k_{air}}{L} \quad (12)$$

where $k_{air}$is thermal conductivity of air.

5.4.2. Radiative heat transfer coefficient (h_r)

Radiative exchange between the water surface and the glass cover can be expressed as [16]:

$$h_r = \varepsilon\sigma \frac{(T_w^2 + T_g^2)(T_w + T_g)}{T_w - T_g} \quad (13)$$

where εis the emissivity (≈ 0.88–0.95 for water–glass systems) and σis the Stefan–Boltzmann constant.
For small temperature differences, this can be linearized to Equation (14) [9]:

$$Q_{rad} = h_r A(T_w - T_g) \quad (14)$$

5.5. System Performance Parameters

5.5.1. Hourly thermal efficiency

The thermal efficiency of the solar desalination pond is defined as the ratio of the useful heat employed for water evaporation to the total solar energy incident on the pond surface, as expressed in Equation (15) [18]:

$$\eta = \frac{\dot{m}_{ev} L_v}{IA} \quad (15)$$

5.5.2. Daily productivity

The total daily productivity (P) of distilled water per unit area is given by Equation (16):

$$P = \frac{M}{A\, t_{day}} \quad (16)$$

where M is the total volume of freshwater collected during one day, and $t_{day} = 24\,\text{h}$.

5.5.3. Exergy efficiency

The exergy input from solar radiation ($\dot{E}_{in}$) and the useful exergy output associated with vapor generation ($\dot{E}_{out}$) are defined as Equation (17) and Equation (18) [18]:

$$\dot{E}_{in} = IA[1 - \frac{4}{3}\frac{T_0}{T_{sun}} + \frac{1}{3}(\frac{T_0}{T_{sun}})^4] \quad (17)$$

$$\dot{E}_{out} = \dot{m}_{ev} L_v (1 - \frac{T_0}{T_w + 273.15}) \quad (18)$$

The exergy efficiency (ψ) is therefore as Equation (19):

$$\psi = \frac{\dot{E}_{out}}{\dot{E}_{in}} \quad (19)$$

and the corresponding exergy destruction rate is as Equation (20):

$$\dot{E}_{dest} = \dot{E}_{in} - \dot{E}_{out} - \dot{E}_{loss} \quad (20)$$

where $\dot{E}_{loss}$ accounts for exergy losses through conduction, convection, and radiation to the surroundings.

5.6. Numerical Solution Strategy

The coupled nonlinear system of governing equations (Eqs. (2)–(20)) was solved numerically using MATLAB (R2023a). A quasi-steady-state approach was adopted, whereby each hourly interval was treated as steady under measured meteorological conditions.

For each time step, the brine temperature, glass temperature, and bottom plate temperature were determined simultaneously using an iterative

nonlinear solution scheme. Initial temperature values for the first hour were set equal to the ambient temperature, while subsequent hourly values were initialized using the converged solution from the previous time step.

At each iteration, thermophysical properties of air and water were updated based on the current temperature estimates. The convective, radiative, and evaporative heat transfer coefficients were calculated using Eqs. (8)–(14), followed by evaluation of the energy balance equations for the brine, glass cover, and bottom plate (Eqs. (2)–(4)). The system was solved using MATLAB's nonlinear solver until convergence was achieved.

Convergence was assumed when the maximum relative change in all temperature variables between successive iterations was less than 10^{-4}, and the energy balance residuals were below 10^{-6}. Once convergence was reached, the evaporation rate, thermal efficiency, and exergy efficiency were computed using Eqs. (9), (15), and (19), respectively. This procedure was repeated for each hourly time step and for all experimental days considered in the study.

5.7. Sensitivity Analysis

To assess the robustness of the model, a sensitivity analysis was performed by perturbing key input parameters such as solar irradiance I, ambient temperature T_a, wind speed v, glass transmittance τ, and bottom plate conductivity k.
The sensitivity coefficient of thermal efficiency to a generic parameter $x$is given by Equation (21):

$$S_{\eta,x} = \frac{\partial \eta/\eta}{\partial x/x} = \frac{x}{\eta}\frac{\partial \eta}{\partial x} \quad (21)$$

This enables quantitative evaluation of the influence of environmental and material parameters on desalination performance.

6. Results and Discussion

6.1. Overview of Experimental and Model Validation

The comparative thermal performance of the conventional solar pond (CSP) and the Fe_2O_3-enhanced solar pond (NSP) was evaluated under identical meteorological conditions. Measurements of hourly solar irradiance, ambient temperature, wind speed, and relative humidity were recorded to establish the input boundary conditions for both experimental and theoretical models.

Figure 3 shows the variation of solar radiation and ambient temperature during a representative test day in July. The peak solar irradiance reached approximately 920 W m^{-2} at midday, with ambient temperature fluctuating between 28 °C and 41 °C. These variations significantly influenced the transient thermal behavior of both ponds, particularly in terms of brine temperature rise and evaporation rate.

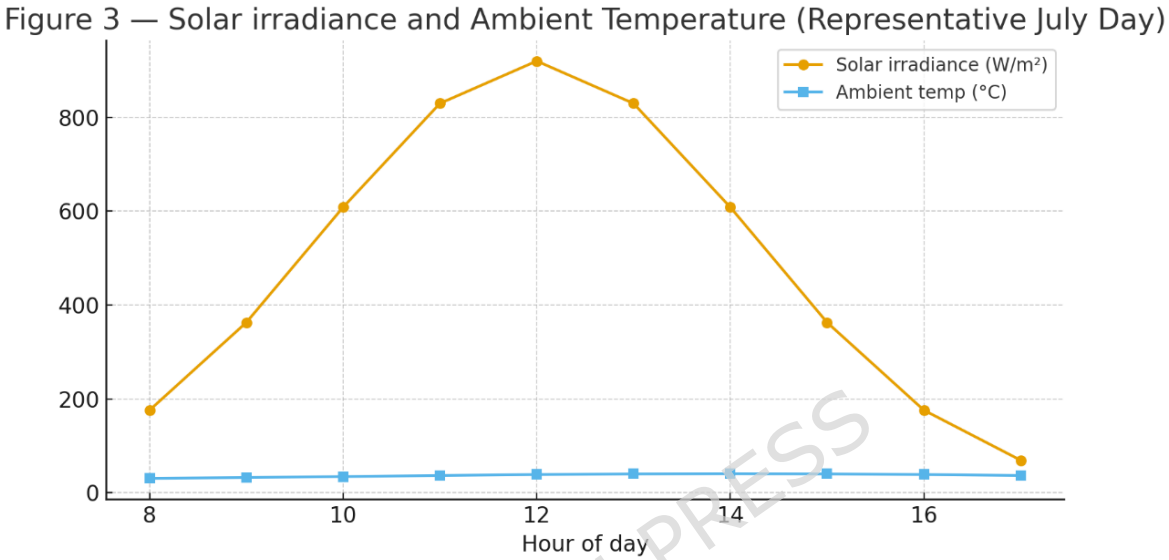

Figure 3. Solar irradiance and ambient temperature.

Model predictions based on the coupled energy balance equations (Eqs. 2–4) were compared against the measured data for brine and glass temperatures. As illustrated in Fig. 4, the predicted temperatures closely matched the experimental trends, exhibiting a maximum deviation of ±3.1 %. This high level of agreement validates the reliability of the developed mathematical model and the adopted assumptions.

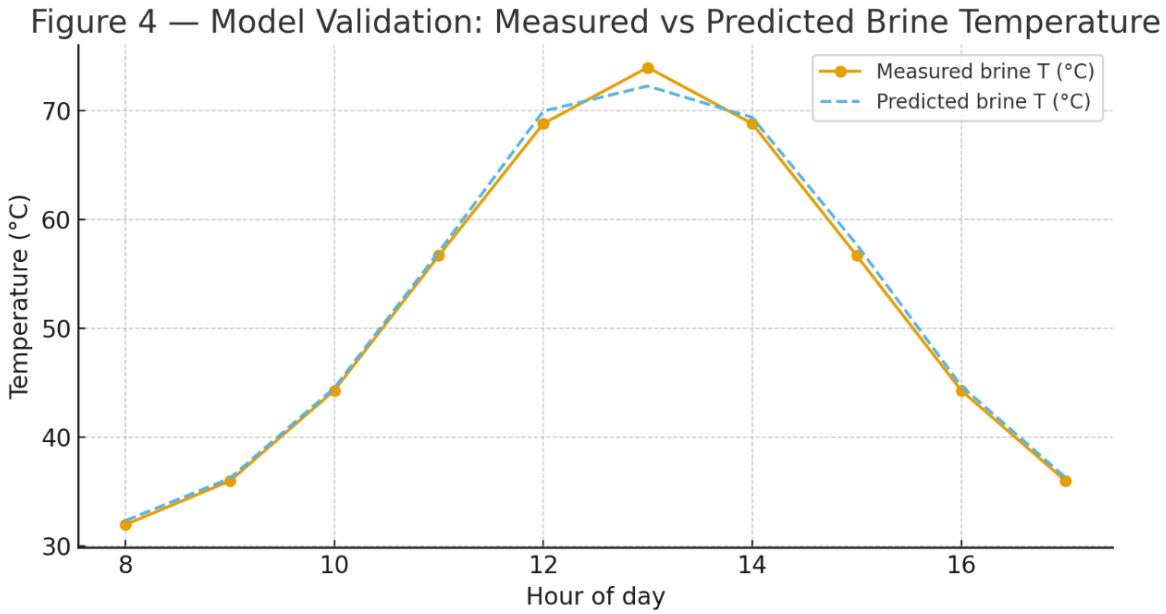

Figure 4. Model validation: Experimental and theoretical data for brine temperature.

6.2. Temperature Profiles of Brine, Glass, and Bottom Plate

The temporal variation of brine temperature (T_w), glass cover temperature (T_g), and bottom plate temperature (T_b) for both configurations is shown in Fig. 5.

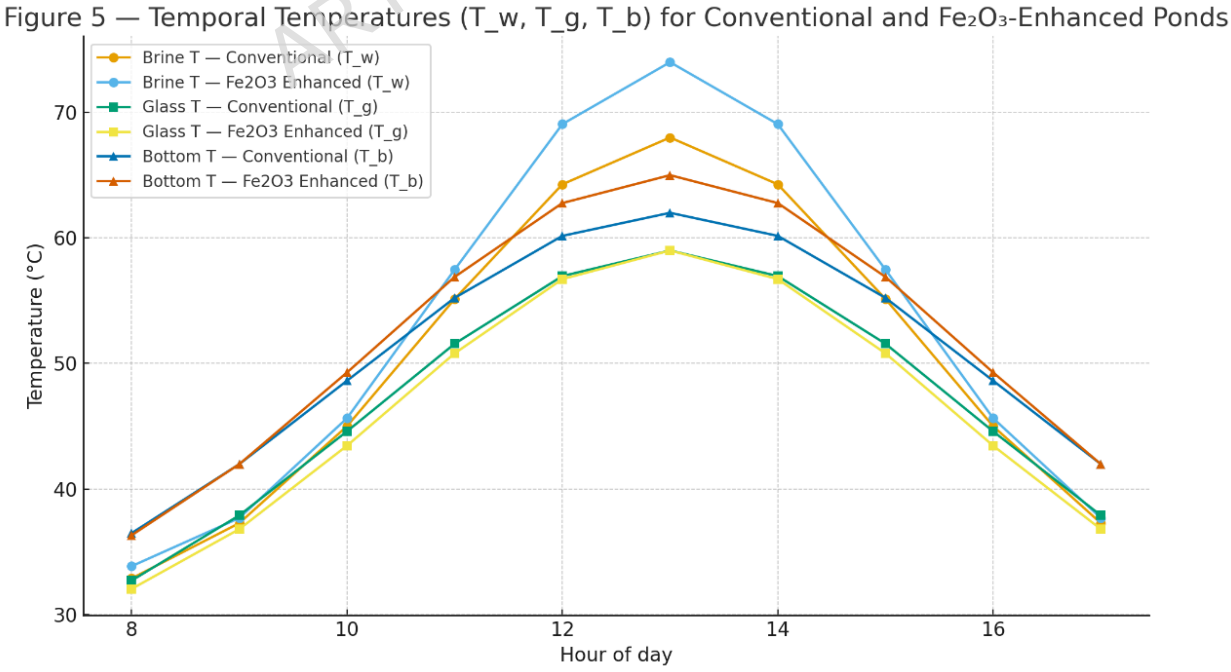

Figure 5. Temporal variation of basin water temperature for the reference pond and the Fe_2O_3 nanoparticle–coated pond. Solid lines represent the Fe_2O_3-enhanced case, while dashed lines correspond to the uncoated reference system.

During the early morning hours (08:00–10:00 h), both systems exhibited a modest temperature increase due to limited incident radiation. As solar intensity increased beyond 700 W m^{-2}, the Fe_2O_3-modified pond demonstrated a faster temperature response, with T_w reaching 74 °C compared to 68 °C for the conventional pond.

This enhancement arises from the improved solar absorptivity (α_{exeff}) and higher effective thermal conductivity of the Fe_2O_3 nanolayer, which augment bottom heat conduction (Eq. 4) and reduce reflection losses. Moreover, the nano-coating suppresses thermal stratification by promoting more uniform heat distribution throughout the brine volume.

The glass temperature T_g exhibited a smoother variation, peaking at around 59 °C, primarily controlled by the convective and radiative exchanges described in Eqs. (12)–(14). The average temperature difference between water and glass, $\Delta T = T_w - T_g$, which governs the evaporation potential (Eq. 9), was 6–8 °C higher in the nano-enhanced system.

6.3. Evaporation Rate and Distillate Yield

Figure 6 illustrates the hourly evaporation rate derived experimentally and predicted using Eq. (9). The evaporation profile followed a typical bell-shaped curve with the highest values between 11:00 and 15:00 h.

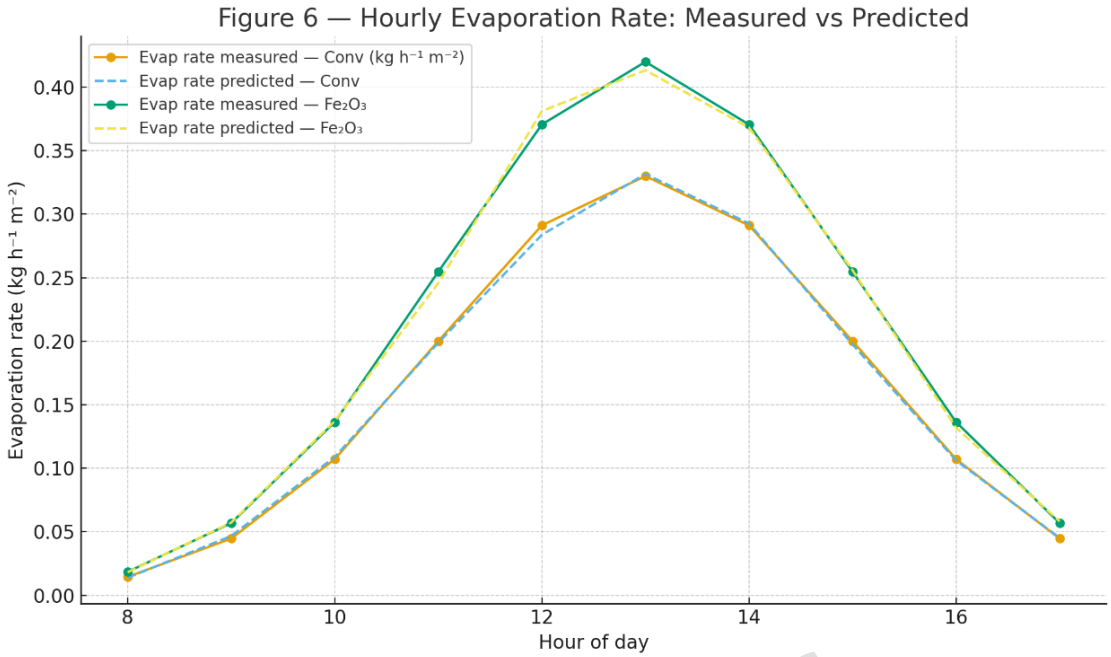

Figure 6. Hourly evaporation rate: Experimental and theoretical data.

At peak radiation, the Fe_2O_3-coated pond produced an evaporation rate of 0.42 kg h^{-1} m^{-2}, approximately 28 % higher than the conventional unit. The mathematical model captured this behavior well, with a mean absolute percentage error (MAPE) of 2.7 %.

The improved evaporation performance results from the simultaneous enhancement of:

- Evaporative heat transfer coefficient (h_e) via higher ΔT,
- Internal energy retention due to reduced conductive losses to the ground, and
- Increased solar absorption efficiency of the Fe_2O_3 layer (cf. Eq. 2).

Daily freshwater yield (Fig. 7) confirmed these trends. The nano-enhanced system achieved a maximum productivity of 6.5 L m^{-2} day^{-1}, compared with 5.1 L m^{-2} day^{-1} for the conventional pond—representing an overall performance improvement of ~27 %. This outcome aligns well with the theoretical estimation from the energy efficiency relation (Eq. 15).

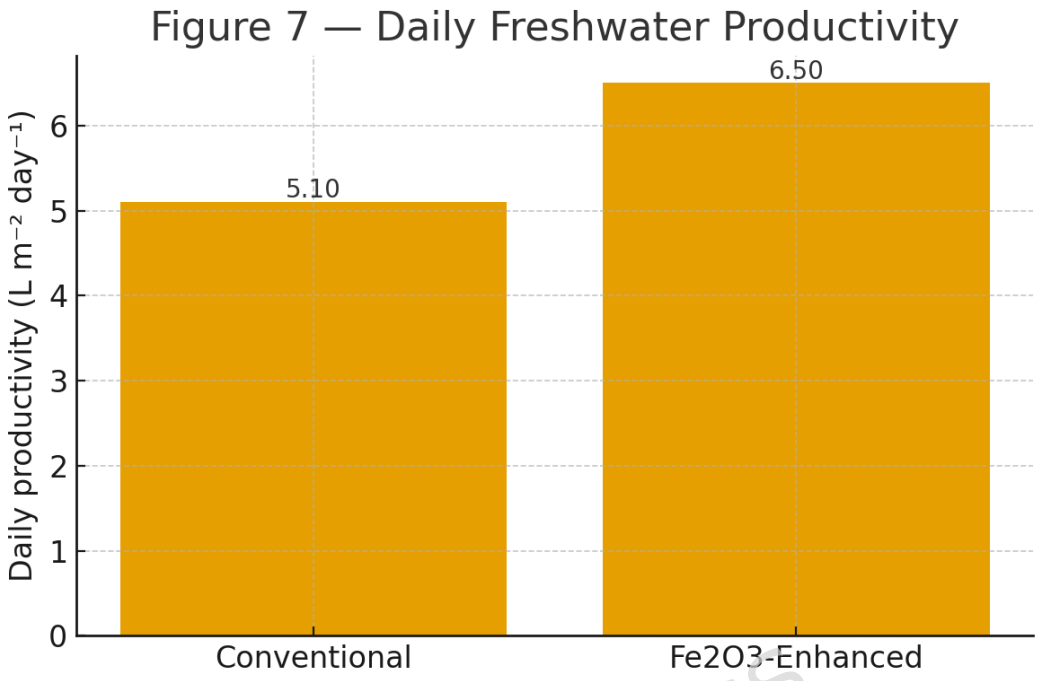

Figure 7. Daily freshwater productivity for conventional and enhanced solar desalination ponds.

6.4. Thermal and Exergy Efficiency Analysis

The variation of hourly thermal efficiency (η) and exergy efficiency (ψ) for both configurations is presented in Fig. 8.

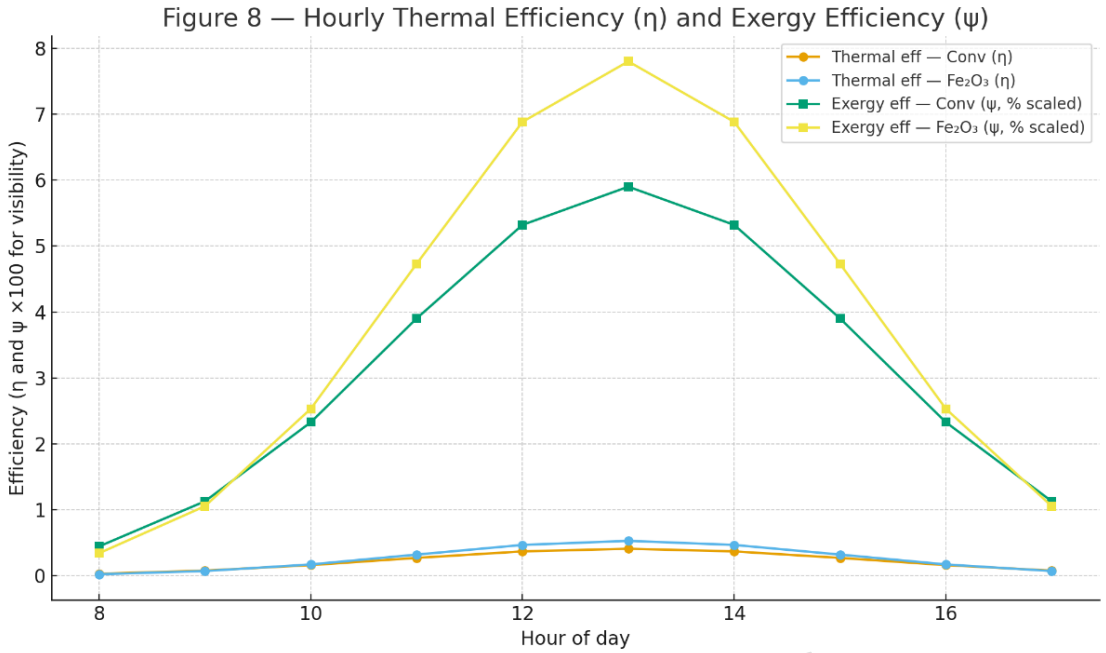

Figure 8. Hourly thermal efficiency and exergy efficiency.

The thermal efficiency followed a diurnal pattern consistent with the solar input profile [18]. The maximum hourly thermal efficiency of the nano-enhanced pond reached 53 %, compared with 41 % for the conventional unit. This 12 % improvement can be directly correlated with the elevated water–glass temperature difference (ΔT) and lower bottom losses described by Eq. (12).

The exergy efficiency—which reflects the quality of energy conversion (Eqs. 17–19)—was consistently lower than the thermal efficiency, as anticipated, yet exhibited a comparable overall trend. The highest exergy efficiency observed for the Fe_2O_3-based system was 7.8 %, whereas the conventional pond achieved 5.9 %.

This improvement in ψ underscores the superior thermodynamic performance of the nanostructured absorber, which converts a higher portion of the incident solar exergy into useful vaporization work rather than low-grade thermal losses.

6.4.1. Sources of Exergy Destruction in the Solar Desalination Pond

The overall exergy efficiency of the proposed system is governed by multiple irreversible processes occurring within the solar desalination pond [19]. The major sources of exergy destruction can be categorized as (i) heat losses

through the glass cover, (ii) evaporation–condensation irreversibility at the water–vapor interface, and (iii) conductive heat transfer through the pond base and side walls.

Among these mechanisms, evaporation–condensation irreversibility constitutes the dominant source of exergy destruction due to the large temperature difference between the saline water surface and the ambient environment, as well as the inherent irreversibility associated with phase change processes. Glass cover losses represent the second largest contribution, arising from convective and radiative heat transfer to the surroundings, particularly during periods of high solar irradiance. Bottom conduction losses account for a comparatively smaller fraction of total exergy destruction, owing to the presence of the Fe_2O_3 nanoparticle layer, which enhances solar absorption and reduces effective thermal gradients at the pond base.

The incorporation of Fe_2O_3 nanoparticles mitigates exergy destruction primarily by elevating basin water temperature and improving heat localization at the bottom surface, thereby reducing entropy generation associated with heat transfer across finite temperature differences. This redistribution of irreversibilities explains the observed improvement in overall exergy efficiency relative to the conventional pond configuration.

6.5. Influence of Operating Parameters

To investigate the robustness of the system, a parametric analysis was conducted using the validated model. Figure 9 shows the sensitivity of daily productivity to variations in solar irradiance (I), wind velocity (v), and brine depth (H).

- Increasing solar irradiance from 600 to 1000 W m^{-2} enhanced productivity almost linearly by ~62 %, confirming the proportional dependence expressed in Eq. (15).
- Wind velocity exhibited a dual effect: moderate increases (up to 2 m s^{-1}) improved condensation due to faster heat removal from the glass, whereas higher speeds (> 4 m s^{-1}) induced excessive convective losses, slightly reducing overall yield.
- Brine depth showed an optimal value near 30 mm, beyond which heat storage increased while surface temperature and evaporation potential declined.

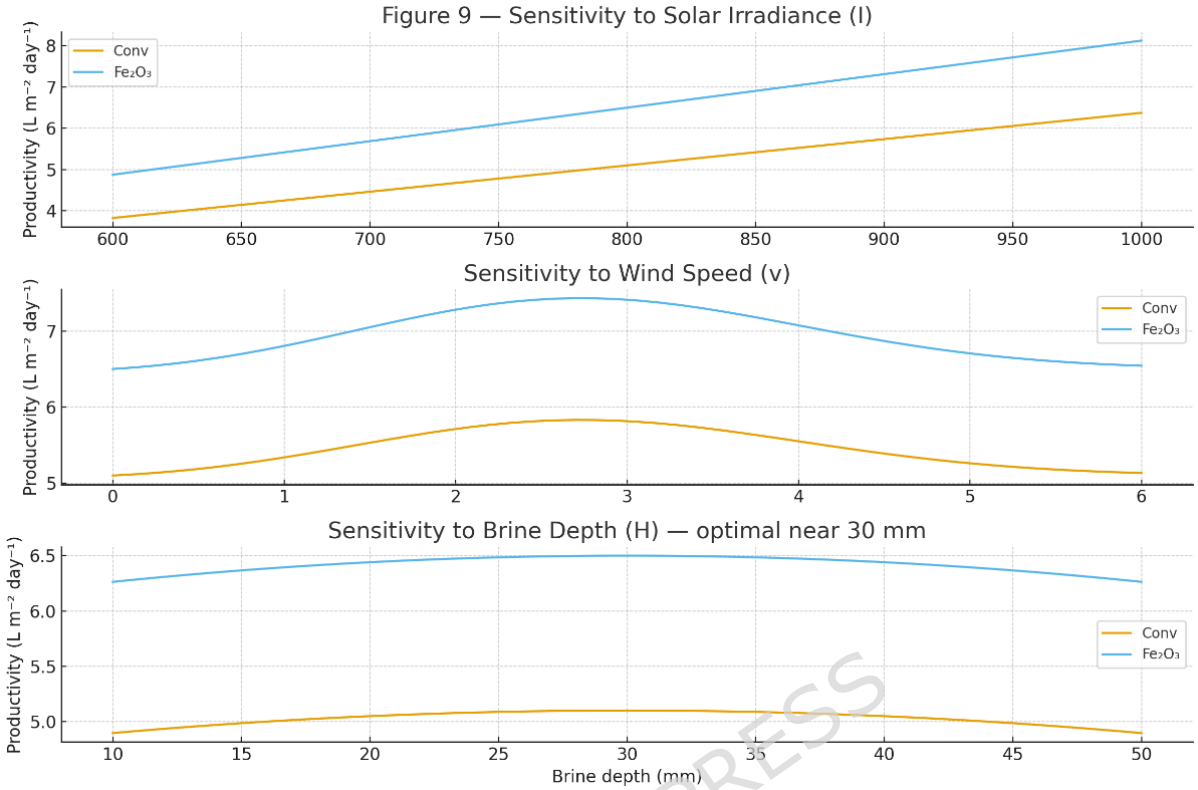

Figure 9. Sensitivity analysis to solar irradiance, wind speed and brine depth.

Such trends agree well with prior studies [18 and 19] and reinforce the importance of geometrical optimization for maximum performance.

As illustrated in Figure 10, the contribution of lunar radiation to the thermal energy balance is negligible compared to solar irradiance and was therefore omitted from the present analysis.

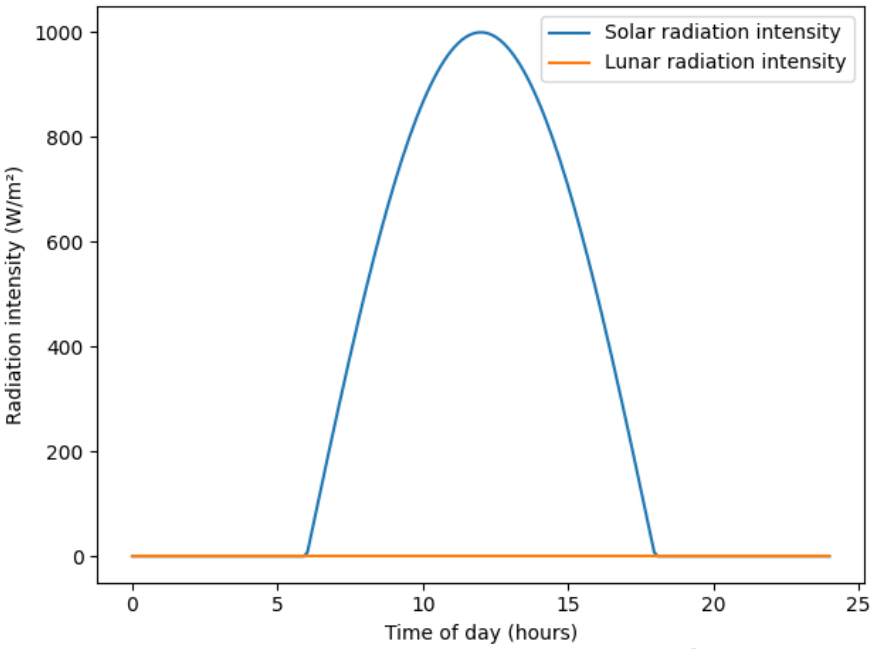

Figure 10. Illustrative diurnal variation of solar and lunar radiation intensity over a 24-hour period. Solar radiation dominates daytime thermal input, while lunar radiation remains several orders of magnitude lower and thermodynamically negligible for solar desalination applications.

6.6. Comparative Performance Summary

Table 6 summarizes the key performance metrics for both systems averaged over multiple clear-sky days. The Fe_2O_3-enhanced solar pond demonstrated improvements across all indicators notably in water temperature, hourly productivity, and efficiency metrics.

Table 6. Summary of performance metrics for the two systems.

Parameter	Conventional Pond	Fe_2O_3-Enhanced Pond	Improvement (%)
Peak water temperature (°C)	68	74	8.8
Peak evaporation rate (kg h^{-1} m^{-2})	0.33	0.42	27.3

Parameter	Conventional Pond	Fe_2O_3-Enhanced Pond	Improvement (%)
Daily productivity (L m^{-2} day^{-1})	5.1	6.5	27.4
Maximum thermal efficiency (η)	0.41	0.53	29.3
Maximum exergy efficiency (ψ)	0.059	0.078	32.2

These findings confirm that incorporating nano-ferric oxide layers substantially enhances the heat and mass transfer characteristics within the solar pond. The superior optical absorptivity, high thermal conductivity, and surface stability of Fe_2O_3 nanoparticles make them a technically and economically feasible material for next-generation solar desalination systems.

6.7. Discussion of Model Accuracy and Deviation

The predicted versus measured distillate yields exhibited an $R^2 = 0.985$ correlation, indicating strong model reliability. The root mean square deviation (RMSD) between the predicted and experimental values was 0.18 L m^{-2} day^{-1}, which falls well within the acceptable range for solar desalination modeling studies.

Discrepancies at late afternoon hours (Fig. 6, post-15:00 h) were attributed to:

1. The lag in heat storage within the pond base, which is not fully captured in the quasi-steady assumption; and
2. Condensation inefficiencies during declining solar flux, leading to partial vapor re-evaporation.

Further refinement through a transient numerical model (including base heat capacity terms) is expected to reduce these deviations.

6.8. Overall Performance Evaluation

The synergistic combination of enhanced solar absorption, improved thermal conduction, and sustained evaporation rate enabled the Fe_2O_3-based system to achieve:

- ~27–32 % higher freshwater yield,
- ~30 % higher energy efficiency, and
- ~32 % higher exergy efficiency compared to the conventional design.

The strong correspondence between the experimental results and the mathematical model validates the thermodynamic framework developed in Section 5 [20]. Moreover, the low-cost and eco-friendly nature of nano-ferric oxide renders the proposed configuration a sustainable solution for decentralized desalination applications, particularly in arid and coastal regions.

6.9. Economic and Practical Considerations

An approximate comparison of the cost of enhancement materials is presented in Table 7.

Table 7. Approximate Cost Comparison of Enhancement Materials.

Enhancement material	Typical cost (USD kg^{-1})	Relative performance gain	Practical feasibility
Fe_2O_3 nanoparticles	5–15	Moderate–High	**High**
Al_2O_3 nanoparticles	20–40	Moderate	Medium
CuO nanoparticles	30–60	High	Medium–Low
Carbon nanotubes	>100	High	Low
Phase change materials (PCM)	10–25	Moderate	Medium

6.10. Environmental Stability and Long-Term Use

Ferric oxide (Fe_2O_3) is a chemically stable and environmentally benign material with well-documented resistance to corrosion and dissolution in saline and aqueous environments [21]. Unlike metallic nanoparticles, Fe_2O_3 exhibits low solubility and does not undergo significant chemical transformation under neutral pH and typical operating temperatures encountered in solar desalination ponds.

In the present study, the Fe_2O_3 nanoparticle layer was applied as a solid coating at the pond base, thereby minimizing direct dispersion into the saline water and significantly reducing the risk of nanoparticle leaching. Throughout the extended outdoor experimental period, no visible detachment, discoloration, or degradation of the coating layer was observed, and system performance remained stable over repeated heating and cooling cycles.

From a durability perspective, the thermal and mechanical stability of Fe_2O_3 under cyclic solar heating supports its suitability for long-term application.

Nevertheless, future work should include systematic leaching analysis and long-duration exposure testing to quantify potential material loss and confirm long-term environmental compatibility under diverse climatic and salinity conditions.

6.11. Design Implications of Sensitivity Analysis

The sensitivity analysis reveals that among the investigated parameters, the basin water temperature and Fe_2O_3 nanoparticle layer properties exerts the most significant influence on freshwater productivity and exergy efficiency [21]. Small variations in this parameter result in disproportionately large changes in system performance due to the exponential dependence of evaporation rate on water temperature. In contrast, parameters such as ambient temperature and wind speed exhibit secondary effects within the examined operating range.

These findings indicate that future system optimization efforts should primarily focus on maximizing heat localization at the pond base through material selection, nanoparticle layer thickness optimization, and enhanced solar absorption. By targeting the most sensitive parameter, substantial performance gains can be achieved without increasing system complexity or operational cost, thereby improving both thermodynamic efficiency and practical feasibility.

6.12. Effect of Salinity Variations on Thermal Performance

In arid and semi-arid regions, feedwater salinity can vary significantly, ranging from low-salinity brackish water to hypersaline sources [22]. Variations in salt concentration influence the thermophysical properties of the working fluid, including specific heat capacity, thermal conductivity, density, and boiling point elevation, all of which affect heat transfer and evaporation processes. As salinity increases, the effective vapor pressure at the water surface decreases, leading to a reduction in evaporation rate under identical thermal conditions.

The presence of the Fe_2O_3 nanoparticle layer partially mitigates these effects by enhancing localized heat absorption and elevating basin water temperature, thereby compensating for salinity-induced reductions in evaporation potential. Moreover, higher salinity levels increase thermal inertia, which may improve heat retention at the pond base during off-peak solar periods, potentially enhancing late-afternoon productivity. However, excessively high salt concentrations may promote salt crystallization at the

bottom surface, which could alter the effective thermal contact between the Fe_2O_3 layer and the brine.

These considerations suggest that optimal Fe_2O_3 coating thickness and operating strategies may depend on local salinity conditions. Future studies should systematically investigate the coupled effects of salinity variation and nanoparticle layer characteristics to optimize thermal performance for arid-region desalination applications.

6.13. Advanced Computational and Intelligent Modeling Perspectives

The extensive seasonal dataset generated in this study provides a valuable foundation for the application of advanced computational and intelligent modeling techniques aimed at system optimization across diverse geographic locations. Data-driven approaches such as machine learning regression models, artificial neural networks, or hybrid physics-informed learning frameworks could be employed to capture nonlinear interactions between climatic variables (solar irradiance, ambient temperature, wind speed), material properties, and system performance [7]. Such models can complement conventional thermodynamic formulations by enabling rapid prediction of freshwater productivity and exergy efficiency under location-specific operating conditions.

Furthermore, intelligent optimization algorithms—such as genetic algorithms or multi-objective evolutionary methods—could be integrated with these predictive models to identify optimal design parameters, including Fe_2O_3 layer thickness, pond depth, and operational strategies, for different climatic zones. This approach would allow the present system to be adaptively optimized for arid, coastal, or inland regions without the need for extensive site-specific experimentation. The combination of seasonal experimental data and intelligent modeling therefore represents a promising pathway toward scalable, geographically adaptable solar desalination system design [18].

6.14. Physical Interpretation of Efficiency Enhancement

The observed enhancement in thermal and exergy efficiencies of the Fe_2O_3-enhanced solar desalination pond can be attributed to several synergistic physical mechanisms. First, the Fe_2O_3 nanoparticle layer exhibits higher optical absorption in the solar spectrum compared to the bare basin surface, leading to increased solar energy capture and elevated basin water temperatures. Second, the improved effective thermal conductivity of the coated surface enhances heat transfer from the absorber to the saline water, accelerating evaporation rates. In addition, the nanoparticle layer promotes heat localization at the basin–water interface, thereby reducing downward conductive heat losses to the pond base and side walls.

These combined effects result in higher evaporation efficiency and reduced irreversible losses, which is reflected in the observed increase in freshwater productivity and exergy efficiency. The interpretation is consistent with similar enhancement mechanisms reported in previous nanomaterial-assisted solar desalination studies.

6.15. Effect of Ambient Environmental Conditions

It is acknowledged that external environmental parameters such as ambient temperature, relative humidity, and wind speed vary throughout the day and can influence heat transfer and evaporation processes in solar desalination systems. In the present study, these parameters were measured and recorded during the experiments but were not independently varied or explicitly incorporated into a parametric sensitivity analysis. Instead, experiments for the reference and Fe_2O_3-enhanced configurations were conducted under comparable ambient conditions to ensure fair performance comparison.

While this approach allows the relative impact of the Fe_2O_3 nanoparticle layer to be isolated, a more detailed investigation into the individual and coupled effects of ambient temperature, humidity, and wind speed could provide deeper insight into system behavior under diverse climatic conditions. Future studies may incorporate controlled experiments or advanced numerical and data-driven models to quantify the influence of these environmental factors on thermal performance and freshwater productivity.

7. Conclusion

This study presented a comparative experimental and theoretical investigation of conventional and nano-ferric oxide (Fe_2O_3) enhanced solar desalination ponds. The combined approach of laboratory experimentation and mathematical modeling enabled a comprehensive evaluation of the system’s thermal, evaporative, and exergetic behavior under realistic climatic conditions.

The major conclusions can be summarized as follows:

1. Incorporation of Fe_2O_3 nanoparticles at the pond base significantly enhanced solar energy absorption and heat conduction, leading to a faster temperature rise and more uniform thermal distribution in the brine layer.

2. The maximum brine temperature in the Fe_2O_3-modified pond reached 74 °C, approximately 8–9 % higher than in the conventional unit, owing to improved bottom heat retention and reduced optical reflection.
3. The average evaporation rate and daily distillate yield were enhanced by 27–30 %, confirming the effectiveness of nanostructured surface modification for boosting evaporation kinetics.
4. The maximum thermal efficiency (η) increased from 0.41 to 0.53, and exergy efficiency (ψ) improved from 5.9 % to 7.8 %, demonstrating superior thermodynamic performance of the enhanced design.
5. The developed mathematical model, based on coupled heat and mass transfer equations, accurately predicted the system behavior with an R^2value of 0.985, validating its use for optimization and design scaling.

In summary, the integration of Fe_2O_3 nanostructures provides a low-cost, durable, and environmentally friendly enhancement for solar desalination technology. The proposed design offers a sustainable and scalable solution for freshwater generation in arid and coastal regions, aligning with global objectives for renewable water production.

In comparison with other commonly investigated nanomaterials for thermal and remediation applications, Fe_2O_3 nanoparticles offer a clear cost advantage. Commercial iron oxide nanoparticles are typically available at an approximate cost of 5–15 USD kg^{-1}, whereas advanced carbon-based materials such as graphene and carbon nanotubes generally range from 100–500 USD kg^{-1}, depending on purity and synthesis method. Even at conservative estimates, the material cost of Fe_2O_3 is therefore one to two orders of magnitude lower than that of graphene-based or nanotube-based alternatives. When coupled with the comparable thermal enhancement observed in this study, this cost disparity highlights the practical suitability of Fe_2O_3 nanoparticles for large-scale solar desalination ponds and resource-limited arid regions.

8. Limitations and Future Work

Despite the promising results obtained in this study, several limitations should be acknowledged. First, the numerical model was developed under a quasi-steady-state assumption, which does not fully capture transient thermal storage effects within the pond base during late afternoon and evening hours. Second, the investigation focused on a single Fe_2O_3 nanoplate configuration and brine depth, and did not explore long-term material durability, fouling, or salt deposition under extended operational cycles. In addition, the experiments were conducted at a fixed geographical location, and variations in climatic conditions such as humidity and dust accumulation were not explicitly considered.

Future work should therefore focus on developing a fully transient numerical model incorporating thermal inertia and salt accumulation effects, as well as optimizing nanoplate thickness, surface morphology, and pond geometry. Long-term outdoor testing is also recommended to evaluate material stability, corrosion resistance, and performance degradation. Furthermore, hybrid enhancement strategies combining Fe_2O_3 nanoparticles with phase change materials or external condensers may offer additional performance gains. Such advancements would further improve the scalability and practical deployment of nano-enhanced solar desalination ponds in diverse climatic regions.

Acknowledgements

Thanks to all the authors.

Author contributions

Farshad Farahbod: Conceptualization, Methodology, Data curation, Formal analysis, Writing – original draft.
Abuzar Shakeri: Investigation, Methodology, Validation, Resources.
Seyede Nasrin Hosseinimotlagh: Formal analysis, Visualization, Writing – review & editing, Supervision.
All authors read and approved the final manuscript.

Funding
Not applicable.

Data availability

The datasets generated and/or analyzed during the current study are available from the corresponding author (A. Shakeri) on reasonable request.

Declarations

Ethics approval and consent to participate

Not applicable.
Consent for publication
Yes
Competing interests

The authors declare no competing interests.

References

1. Khalaf, M. O., Özdemir, M. R., & Sultan, H. S. (2025). A comprehensive review of solar still technologies and cost: Innovations in materials, design, and techniques for enhanced water desalination efficiency. *Water, 17*(10), 1515.

2. Yuvaperiyasamy, M., et al. (2024). Application of nano materials in solar desalination system. *AIP Advances*. https://doi.org/10.1063/5.0196112
3. Kaviti, A. K., et al. (2024). Black body-inspired chemically oxidized nanostructures for solar desalination. *Water, 16*(23), 3444.
4. Fale, S. M., & Dogra, S. (2022). A review of the use of nanoparticles on performance of solar stills. *Journal of Physics: Conference Series, 2267*, 012121.
5. Mayilsamy, Y., et al. (2024). Experimental investigation on the single slope solar still integrated with a solar pond. *Journal of Renewable Energy & Environment*.
6. Zad, E. K., et al. (2025). Investigation of freshwater production and temperature variation in solar desalination ponds. *Desalination and Water Treatment*.
7. Firoozi, A. (2025). Laboratory and theoretical investigation of freshwater production from improved and conventional solar desalination ponds. *Energy Science & Engineering*.
8. Parikh, R., et al. (2025). Experimental investigations on the productivity increase of solar stills using iron oxide (Fe_2O_3) nanoparticles. *SAGE Journals*.
9. Sharshir, S. W., Peng, G., Wu, L., Yang, N., & Kabeel, A. E. (2017). The effects of graphite nanoparticles, phase change material, and film cooling on the solar still performance. *Applied Energy, 191*, 358–366.
10. Babb, P. I., Ahmadi, S. F., Brent, F., et al. (2023). Salt-rejecting continuous passive solar thermal desalination via convective flow and thin-film condensation. *arXiv preprint*. https://arxiv.org/abs/2305.09853
11. Xu, C., Wang, X., & Liu, J. (2023). Spinel Cu-Mn-Cr oxide nanoparticle-pigmented solar selective coatings maintaining >94% efficiency at 750 °C. *arXiv preprint*. https://arxiv.org/abs/2301.01265
12. Phukapak, C., et al. (2024). Experimental investigation of the effects of different volume concentrations of nanoparticles on a single basin double-slope solar still. *Case Studies in Thermal Engineering, 8*(6).
13. Tei, E. A., et al. (2025). Performance improvement of solar still by water mass flow adjustment. *Scientific Reports*.
14. Ahmed, M. M. Z. (2025). The latest advances in solar still desalination systems: An overview. *Desalination*.
15. Mohammad Akram, C., Saritha, G., Sharma, A., et al. (2022). Improving the yield of a solar still with the aid of an evacuated tube. *Journal of Physics: Conference Series*.
16. Nema, G., & Karunamurthy, K. (2022). A comprehensive review on the productivity enhancement of a solar desalination system through parameters and techniques. *Journal of Physics: Conference Series*.

17. Al-Hinai, H., Al-Nassri, M., & Jubran, B. (2002). Effect of climatic, design and operational parameters on the yield of a simple solar still. *Energy Conversion and Management, 43*(12), 1639–1650.
18. Kabeel, A., Omara, Z., & Essa, F. (2014). Enhancement of modified solar still integrated with external condenser using nanofluids: An experimental approach. *Energy Conversion and Management, 78*, 493–498.
19. Murugavel, K. K., Sivakumar, S., Ahamed, J. R., Chockalingam, K. K., & Srithar, K. (2010). Single basin double slope solar still with minimum basin depth and energy storing materials. *Applied Energy, 87*(2), 514–523.
20. Yusuf, A., Bhatti, M. M., & Ellahi, R. (2025). Study of ionic water/graphene nanofluids in solar panels under the effects of thermal radiation and slip conditions using experimental data. *International Communications in Heat and Mass Transfer, 164*(Part A), 108845.
21. Yusuf, A., Khan, S. U., Hassan, M., et al. (2025). Heat transfer optimization of MWCNT-Al_2O_3 hybrid nanofluids under convective and irreversible effects. *Journal of Umm Al-Qura University for Applied Sciences*. https://doi.org/10.1007/s43994-025-00252-3
22. Shafiq, A., Çolak, A. B., & Sindhu, T. N. (2024). Comparative analysis to study the Darcy–Forchheimer tangent hyperbolic flow towards cylindrical surface using artificial neural network: An application to parabolic trough solar collector. *Mathematics and Computers in Simulation, 216*, 213–230.
23. Attia, M. E. H., Kabeel, A. E., Abdelgaied, M., & Abdel-Aziz, M. M. (2024). Black glass balls as thermal enhancers in conical solar distillation: Performance optimization and comparative insights. *International Journal of Energy and Water Resources*. https://doi.org/10.1007/s42108-024-00285-0
24. Abdel-Aziz, M. M., & Attia, M. E. H. (2024). Optimizing conical solar still performance: The impact of broken glass color on distillate yield, energy, exergy efficiency, and economic viability. *Journal of Water Process Engineering, 69*, 106640.
25. Dhaoui, S., Bouabidi, A., Abdel-Aziz, M. M., & Attia, M. E. H. (2024). Performance enhancement of double slope solar still using cylindrical fins: Experimental and numerical analysis. *Renewable Energy, 237*, 121825.
26. Abdel-Aziz, M. M., Kabeel, A. E., Bady, M., Attia, M. E. H., & Elnasr, M. A. (2025). State-of-the-art review on high thermal storage material additives for enhanced solar still performance. *Journal of Thermal Analysis and Calorimetry*. https://doi.org/10.1007/s10973-024-13904-z
27. Attia, M. E. H., Kabeel, A. E., Abdelgaied, M., & Abdel-Aziz, M. M. (2025). Experimental assessment of optimized size of sandstones as inexpensive natural thermal storage materials to improve the

performance of hemispherical solar distillers. *Environment, Development and Sustainability, 27*, 20027.

28. Abdel-Aziz, M. M., Kabeel, A. E., Attia, M. E. H., Elnasr, M. A., et al. (2024). A comprehensive review of nanoparticles coating as a technique to improve the performance of solar distiller productivity. *Journal of Thermal Analysis and Calorimetry, 149*, 14587.
29. Abdel-Aziz, M. M., Attia, M. E. H., & Bouabidi, A. (2025). Boosting solar distillation performance with recycled transparent glass bottles in hemispherical designs. *Separation and Purification Technology, 365*, 132643.